Science

AAAS

RIM-Binding Protein, a Central Part of the Active Zone, Is Essential for Neurotransmitter Release

Karen S. Y. Liu *et al.*
Science **334**, 1565 (2011);
DOI: 10.1126/science.1212991

This copy is for your personal, non-commercial use only.

---

diets to control the formation of immune system components (*29*) and the composition of the microbiota (*32*). Plant-derived phytochemicals seem to enhance the pool of RORγt⁺ ILC, and derivative compounds may be used in the future to therapeutically modulate their function in the context of necrotizing enterocolitis of pre-term infants (*33*) and intestinal inflammatory diseases (*4*).

References and Notes

1. D. Artis, *Nat. Rev. Immunol.* **8**, 411 (2008).
2. L. V. Hooper, A. J. Macpherson, *Nat. Rev. Immunol.* **10**, 159 (2010).
3. S. L. Sanos, C. Vonarbourg, A. Mortha, A. Diefenbach, *Immunology* **132**, 453 (2011).
4. K. J. Maloy, F. Powrie, *Nature* **474**, 298 (2011).
5. Y. Kanamori et al., *J. Exp. Med.* **184**, 1449 (1996).
6. G. Eberl, D. R. Littman, *Science* **305**, 248 (2004).
7. O. Pabst et al., *Eur. J. Immunol.* **35**, 98 (2005).
8. M. Tsuji et al., *Immunity* **29**, 261 (2008).
9. D. Bouskra et al., *Nature* **456**, 507 (2008).
10. S. L. Sanos et al., *Nat. Immunol.* **10**, 83 (2009).
11. C. Luci et al., *Nat. Immunol.* **10**, 75 (2009).
12. N. Satoh-Takayama et al., *Immunity* **29**, 958 (2008).
13. M. Cella et al., *Nature* **457**, 722 (2009).
14. C. Vonarbourg et al., *Immunity* **33**, 736 (2010).
15. L. Eckmann, *Ann. N. Y. Acad. Sci.* **1072**, 28 (2006).
16. Y. Zheng et al., *Nat. Med.* **14**, 282 (2008).
17. G. F. Sonnenberg, L. A. Monticelli, M. M. Elloso, L. A. Fouser, D. Artis, *Immunity* **34**, 122 (2011).
18. B. E. McIntosh, J. B. Hogenesch, C. A. Bradfield, *Annu. Rev. Physiol.* **72**, 625 (2010).
19. R. A. Dixon, *Annu. Rev. Plant Biol.* **55**, 225 (2004).
20. Materials and methods are available as supporting material on *Science* Online.
21. R. E. Mebius, *Nat. Rev. Immunol.* **3**, 292 (2003).
22. M. Veldhoen et al., *Nature* **453**, 106 (2008).
23. F. J. Quintana et al., *Nature* **453**, 65 (2008).
24. S. Sawa et al., *Science* **330**, 665 (2010).
25. S. A. Luther, K. M. Ansel, J. G. Cyster, *J. Exp. Med.* **197**, 1191 (2003).
26. S. Chappaz, C. Gärtner, H.-R. Rodewald, D. Finke, *J. Immunol.* **185**, 3514 (2010).
27. L. F. Bjeldanes, J. Y. Kim, K. R. Grose, J. C. Bartholomew, C. A. Bradfield, *Proc. Natl. Acad. Sci. U.S.A.* **88**, 9543 (1991).
28. M. Lochner et al., *J. Exp. Med.* **208**, 125 (2011).
29. Y. Li et al., *Cell* **147**, 629 (2011).
30. L. Puddington, S. Olson, L. Lefrançois, *Immunity* **1**, 733 (1994).
31. M. Burow, B. A. Halkier, D. J. Kliebenstein, *Curr. Opin. Plant Biol.* **13**, 347 (2010).
32. J. J. Faith, N. P. McNulty, F. E. Rey, J. I. Gordon, *Science* **333**, 101 (2011).
33. J. Neu, W. A. Walker, *N. Engl. J. Med.* **364**, 255 (2011).

RIM-Binding Protein, a Central Part of the Active Zone, Is Essential for Neurotransmitter Release

Karen S. Y. Liu,[1]* Matthias Siebert,[2]* Sara Mertel,[1]* Elena Knoche,[2]*
Stephanie Wegener,[2]* Carolin Wichmann,[2] Tanja Matkovic,[1] Karzan Muhammad,[1]
Harald Depner,[1] Christoph Mettke,[1] Johanna Bückers,[3] Stefan W. Hell,[3] Martin Müller,[4]
Graeme W. Davis,[4] Dietmar Schmitz,[2,5]† Stephan J. Sigrist[1,2]†

The molecular machinery mediating the fusion of synaptic vesicles (SVs) at presynaptic active zone (AZ) membranes has been studied in detail, and several essential components have been identified. AZ-associated protein scaffolds are viewed as only modulatory for transmission. We discovered that *Drosophila* Rab3-interacting molecule (RIM)–binding protein (DRBP) is essential not only for the integrity of the AZ scaffold but also for exocytotic neurotransmitter release. Two-color stimulated emission depletion microscopy showed that DRBP surrounds the central Ca²⁺ channel field. In *drbp* mutants, Ca²⁺ channel clustering and Ca²⁺ influx were impaired, and synaptic release probability was drastically reduced. Our data identify RBP family proteins as prime effectors of the AZ scaffold that are essential for the coupling of SVs, Ca²⁺ channels, and the SV fusion machinery.

In response to Ca²⁺ influx, synaptic vesicles (SVs) fuse with the active zone (AZ) membrane. An elaborate protein-based cytomatrix covering the AZ membrane is meant to facilitate the release process, but its components and operational principles are poorly understood (*1–4*). We previously found Bruchpilot to be an essential building block of the *Drosophila* AZ cytomatrix (the T bar) (*5*). Here, we used antibodies to screen for additional cytomatrix components.

Rab3-interacting molecule (RIM)–binding proteins (RBPs) are enriched at presynaptic terminals (*6–8*) and interact with voltage-gated Ca²⁺ channels (VGCCs). Mammals harbor three *rbp* family loci; *Drosophila* has a single *rbp* gene (*drbp*) (*9*). We generated antibodies against *Drosophila* RBP (DRBP) (epitopes in Fig. 1A), which stained presynapses at neuromuscular junctions (NMJs) (Fig. 1B, left). The size of AZ cytomatrices is below the diffraction limit of light microscopy.

To overcome this, we used a two-color stimulated emission depletion (STED) (*10*) microscope providing 50-nm resolution in the focal plane (Fig. 1B, right) (*11*). Relative to the Bruchpilot C-terminal label, DRBP C-terminal immunoreactivity localized toward the AZ center (Fig. 1C, left; model: Fig. 1F). Vertically, the DRBP label localized ~100 nm closer to the AZ membrane than the Bruchpilot C-terminal label (Fig. 1C, right; quantification in Fig. 1F). Postembedding immunogold labeling against DRBP C terminus yielded similar results (fig. S1). DRBP C- and N-terminal labels are similarly distributed in planar views (compare Fig. 1C and 1D, left), and in vertical views the centers of the DRBP C- and N-terminal signals are on average ~30 nm apart (compare Fig. 1C and 1D, right). The Cacophony (Cac) VGCC (*12, 13*) localizes beneath the scaffold formed by Bruchpilot in the AZ center (*14*). DRBP C terminus encircled a small (50 to 100 nm) AZ-central field of Cac^GFP (with green fluorescent protein) (*12, 15*) (Fig. 1E, left).

We subjected the *drbp* locus to genetic analysis (fig. S2). A strain with a transposon inserted between exons 6 and 7 (MB02027, *drbp*^Minos^) was positioned in trans over a deficiency including *drbp*, as well as a neighboring locus [Df(3R) S201, short *Df*, see fig. S2]. In these larvae, DRBP levels at NMJs were reduced to one-third of control levels (Fig. 2A) (*drbp*^Minos^; arbitrary fluorescence intensity 36% ± 2, n = 27; control 100% ± 2, n = 21; P > 0.0001, Mann-Whitney U test). These *drbp* hypomorphic flies hatched below expected Mendelian ratios, and mutant larvae showed reduced locomotion (fig. S3). Chemical mutagenesis screening provided alleles with premature stop codons (*drbp*^STOP1^, *drbp*^STOP2^, and *drbp*^STOP3^) (Fig. 1A and fig. S2). Animals carrying these alleles over *Df* only rarely reached adulthood, and mutant larvae barely moved

[1]Department of Genetics, Institute for Biology, Free University Berlin, 14195 Berlin, Germany. [2]NeuroCure Cluster of Excellence, Charité Berlin, Charitéplatz 1, 10117 Berlin, Germany. [3]Department of Nanobiophotonics, Max Planck Institute for Biophysical Chemistry, Am Fassberg 11, 37077 Göttingen, Germany. [4]Department of Biochemistry and Biophysics, University of California San Francisco, San Francisco, CA 94158, USA. [5]DZNE—German Center for Neurodegenerative Diseases, 10117 Berlin, Germany.

*These authors contributed equally to this work.
†To whom correspondence should be addressed. E-mail: dietmar.schmitz@charite.de (D.S.); stephan.sigrist@fu-berlin.de (S.J.S.)

(fig. S3). DRBP immunoreactivity at mutant larval NMJs was completely absent when we used either N- (fig. S4) or C-terminal antibodies (Fig. 2A). Thus, we consider these alleles to be null. Using pacman technology (*16*), we produced a genomic transgene encompassing the entire *drbp* locus (Rescue) (fig. S2). One copy of this construct partially restored NMJ staining (Fig. 2A) and partially rescued *drbp*$^{STOP1-3}$ adult vitality. Mutant larval NMJ terminals reached normal morphological size (Fig. 2B) (control: 516 ± 51 μm^2, *n* = 20; *drbp*^{STOP1}: 554 ± 41 μm^2, *n* = 20; *P* = 0.4903, Mann-Whitney *U* test), and had normal synapse numbers (Fig. 2B) (control: 454 ± 39, *n* = 20; *drbp*^{STOP1}: 489 ± 34, *n* = 20; *P* = 0.36, Mann-Whitney *U* test), as also seen in transmission electron microscopy (TEM) (fig. S5A, arrows). Postsynaptic glutamate receptor (GluR) fields appeared enlarged (Fig. 2B).

Bruchpilot spots in *drbp* mutants appeared largely unaltered at confocal resolution (Fig. 2B). However, with STED, Bruchpilot signals emerged as atypically organized, no longer forming regular donuts but adopting irregular shapes (compare Fig. 2C, arrows left to right). Bruchpilot signals extended into the cytoplasm unusually far

(Fig. 2C, asterisks), not matching postsynaptic GluR fields in either planar (Fig. 2C, arrows) or vertical views (Fig. 2C, arrowheads). Organization of the AZ cytomatrix in *drbp* mutants was clearly affected in electron microscopy (EM) of both conventionally embedded samples (fig. S5B) and high-pressure frozen- and freeze-substituted (HPF) (*14, 17, 18*) samples (Fig. 2D). The *drbp* hypomorph (*drbp*^{Minos}/*Df*) still formed structures resembling T-bar platforms (Fig. 2D, arrows), but they resided on thinner pedestals (Fig. 2D, arrowheads) (T-bar width: controls = 85.5 ± 10, *drbp*^{Minos} = 56.3 ± 5.5, *P* < 0.05; T-bar height: controls = 55.8 ± 1.4, *drbp*^{Minos} = 48.5 ± 2.2, *P* < 0.01, Student's *t* test). At AZ membranes of *drbp* nulls, abnormally shaped electron-dense material was found, but no regular T bars (Fig. 2D). In three-dimensional electron tomography reconstructions, it became obvious that the entire cytomatrix was severely misshapen (Fig. 2E). We occasionally observed free-floating electron-dense material detached from the AZ plasma membrane in *drbp* nulls (fig. S5, C and D). These atypical electron densities still tethered SVs (fig. S5B, arrows; insets in fig. S5, C and D), a function mediated by the C-terminal end of Bruch-

pilot (*19*). With EM, overall SV density in NMJ boutons appeared unaltered (fig. S5A). The number of membrane-proximal SVs (up to a 5-nm distance) counted over the whole AZ, however, were reduced in *drpb*^{STOP1} animals [control: 3.2 ± 0.2, *n* of AZs = 26; *drbp*^{Minos}: 3.1 ± 0.3, *n* of AZs = 17, *P* = 0.79; *drbp*^{STOP1}: 2.1 ± 0.3, *n* of AZs = 16; *P* < 0.005, Student's *t* test; scored with HPF, as standard aldehyde fixation is imprecise for this purpose (*20*)]. For functional analysis, two-electrode voltage-clamp recordings were performed at larval NMJs. In *drbp* hypomorphs, evoked excitatory junctional current (eEJCs) amplitudes were reduced by about half (Fig. 3A). In *drbp* nulls, synaptic transmission was practically abolished (Fig. 3A) [control: –52.4 ± 4.9 nA, *n* = 10; *drbp*^{STOP1}: –2.6 ± 0.2 nA, *n* = 4; *drbp*^{Minos}: –23.0 ± 5.3 nA, *n* = 8; *P* < 0.001; one-way analysis of variance (ANOVA) Tukey's post test]. We facilitated synaptic release by recording in elevated extracellular Ca^{2+}. In 2 mM Ca^{2+}, eEJC amplitudes were reduced to ~10% of control levels in all three null alleles. One copy of the genomic *drbp* transgene (fig. S2) completely rescued this phenotype (Fig. 3B) (control: –113.7 ± 7.2 nA, *n* = 12; *drbp*^{STOP1}: –11.7 ± 2.8 nA,

Fig. 1. Two-color STED analysis of DRBP organization at *Drosophila* NMJ synapses. (**A**) DRBP entails 3 Src homology 3 (SH3) domains interrupted by fibronectin type 3 (FN3) domains. The third SH3 domain interacts with both RIM and Ca^{2+} channels in yeast two-hybrid experiments (fig. S6). Positions of STOP codons introduced by chemical mutagenesis and antibody (Ab)–binding epitopes (AB) are shown (based on Flybase CG43073-PB). (**B**) Synaptic boutons stained with the indicated Abs showing AZs in planar [arrow, magnification in (C), left] and vertical [arrowhead, magnification in (C), right] views with confocal (left) and STED (right) resolution. (**C** to **E**) STED images of individual planar (left) and vertical (right) AZs stained with the indicated Abs. (**F**) Model of an AZ in oblique view, with peak-to-peak vertical distance measurements performed on two-color STED images. PRE, presynaptic, POST, postsynaptic. Scale bars: (B) 1.5 μm; (C to E) 200 nm.
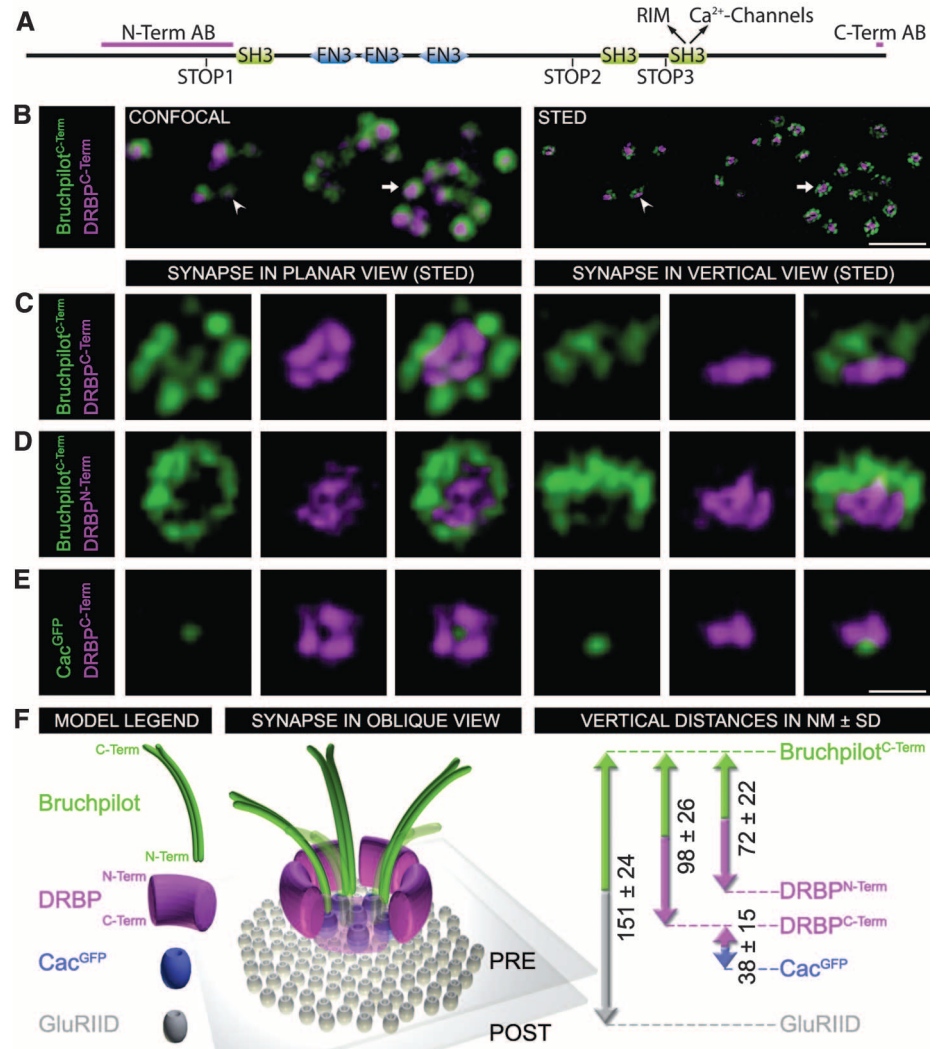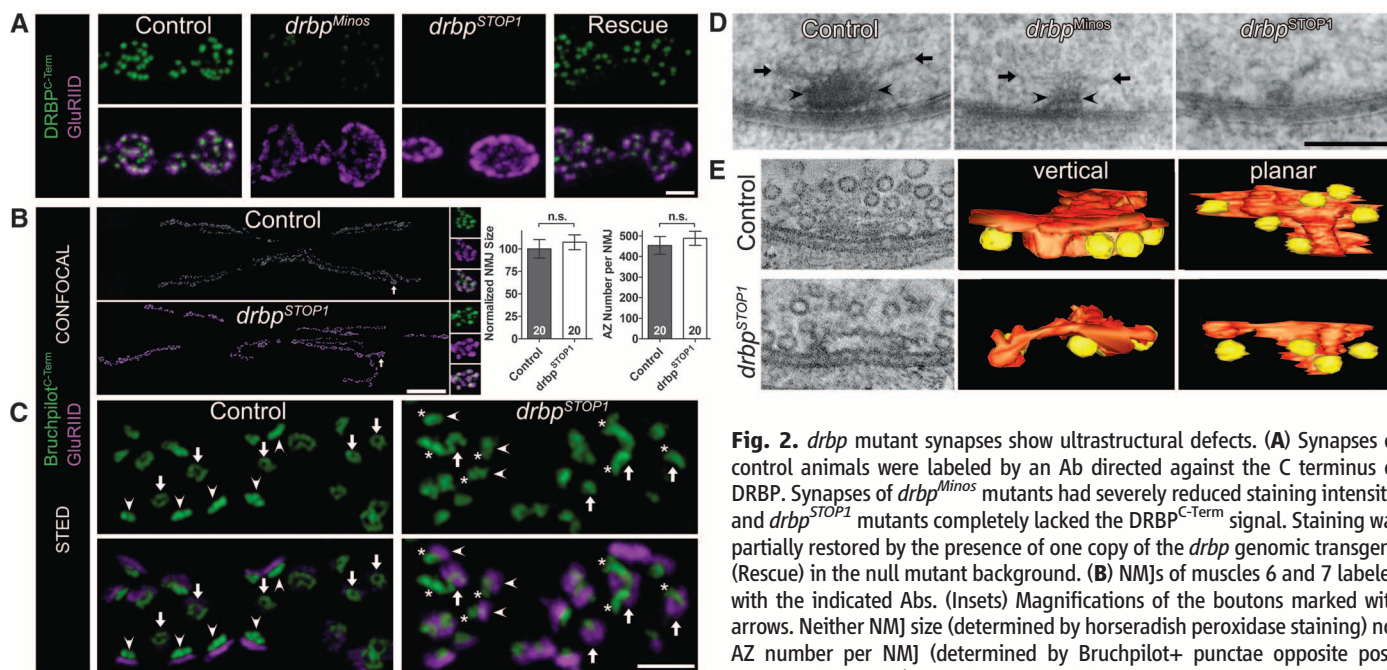
$n = 9$; $drbp^{STOP2}$: -9.8 ± 3.1 nA, $n = 6$; $drbp^{STOP3}$: -9.6 ± 1.6 nA, $n = 8$; Rescue: -119.1 ± 12.7 nA, $n = 7$; $P < 0.001$; one-way ANOVA, Tukey's post test). Frequency and amplitude of miniature excitatory junctional currents (mEJCs) were unchanged in $drbp^{STOP1}$ (Fig. 3C), despite enlarged GluR fields. Thus, the number of quanta (i.e., SVs) released per individual action po-

tential (AP) (quantal content, Fig. 3D) was dramatically reduced in the absence of DRBP.

At paired-pulse stimulation, $drbp^{STOP1}$ synapses exhibited an unusually strong facilitation (Fig. 4A). During a 10-Hz stimulation train, a protocol that leads to marked depression of eEJCs in controls, $drbp^{STOP1}$ mutants showed sustained facilitation and reached a steady-state level more

than double the initial amplitude (Fig. 4B). When stimulated with five consecutive pulses at 100 Hz, $drbp^{STOP1}$ eEJCs exhibited substantial recovery and almost reached absolute control levels on the fifth pulse (Fig. 4C). Altogether, these results suggest that $drbp$ null mutants suffer from a severely reduced release probability. However, as SV release can be substantially elevated under

Fig. 2. $drbp$ mutant synapses show ultrastructural defects. (**A**) Synapses of control animals were labeled by an Ab directed against the C terminus of DRBP. Synapses of $drbp^{Minos}$ mutants had severely reduced staining intensity, and $drbp^{STOP1}$ mutants completely lacked the DRBP^{C-Term} signal. Staining was partially restored by the presence of one copy of the $drbp$ genomic transgene (Rescue) in the null mutant background. (**B**) NMJs of muscles 6 and 7 labeled with the indicated Abs. (Insets) Magnifications of the boutons marked with arrows. Neither NMJ size (determined by horseradish peroxidase staining) nor AZ number per NMJ (determined by Bruchpilot+ punctae opposite post-synaptic GluR fields) were changed in $drbp$ mutants compared with controls. Means ± SEM. n.s., Not significant ($P > 0.05$). (**C**) STED images of synapses stained with the indicated Abs. Control synapses showed typical donut-shaped Bruchpilot^{C-Term} signals in planar views (arrows, left), whereas in $drbp$ mutants Bruchpilot^{C-Term} signal appeared misshapen (arrows, right). In vertical views, Bruchpilot^{C-Term} and GluR subunit IID (GluRIID) labels were strictly opposed (arrowheads, left), whereas in $drbp$ mutants, Bruchpilot^{C-Term} signal often extended unusually far into the cytoplasm (arrowheads, right; ectopic material marked by asterisks). (**D**) T-bar EM images from controls, $drbp^{Minos}$ and $drbp^{STOP1}$ NMJs. T-bar pedestals marked with arrowheads and T-bar platforms with arrows. In $drbp^{Minos}$, T bars appeared thinner, whereas $drbp^{STOP1}$ synapses lacked normally shaped T bars. (**E**) Electron tomography of control and $drbp^{STOP1}$ T bars. (Left) Virtual single section from reconstructed tomogram. Rendered model is shown in the middle (vertical view) and on the right (planar view from the bottom on the pedestal). Red, T bar; yellow, membrane proximal SVs. Scale bars: (A) 2 μm; (B) 20 μm, overview, 6 μm, insets; (C) 1 μm; (D) 100 nm.

Fig. 3. $drbp$ mutants suffer from defective evoked neurotransmitter release. (**A**) eEJC sample traces and quantification for control, $drbp^{Minos}$, and $drbp^{STOP1}$ (1 mM extracellular Ca^{2+}, 0.2 Hz). (**B**) eEJC sample traces and quantification for control, $drbp$ null mutants, and genomic rescue recorded at 2 mM extracellular Ca^{2+}. (**C**) (Left) mEJC sample traces. (Middle) Mean cumulative histogram of mEJC amplitudes (mean ± standard deviation; two-tailed Kolmogorov-Smirnov test: $P = 0.89$). (Right) mEJC frequency (control: 0.92 ± 0.14, $n = 10$; $drbp^{STOP1}$: 1.01 ± 0.19, $n = 11$; Student's t test: $P = 0.72$). (**D**) Quantal content of $drbp^{STOP1}$ eEJCs was significantly reduced (control: 120.8 ± 6.9, $n = 9$; $drbp^{STOP1}$: 9.5 ± 1.8, $n = 11$; $P < 0.001$; Student's t test). Means ± SEM (unless otherwise noted).
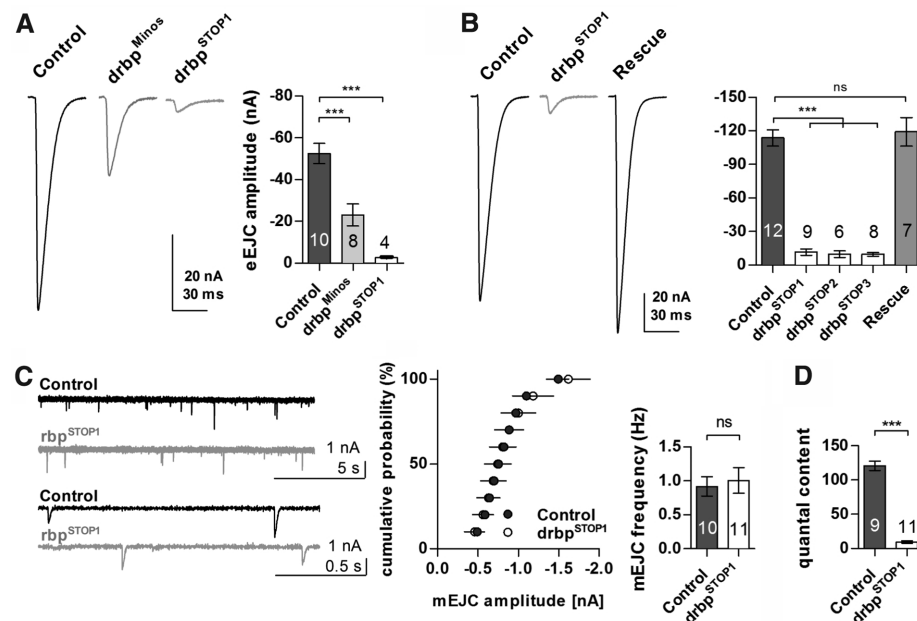
high-frequency stimulation, we conclude that the core fusion machinery is still operational in *drbp* mutants, and we hypothesize that the reduced SV release evoked by single APs is mainly due to defects upstream of the SV fusion process.

The eEJC rise times were slightly but significantly increased (Fig. 4D) (control 1.00 ± 0.05 ms, $n = 12$; $drbp^{STOP1}$ 1.34 ± 0.09 ms, $n = 9$; $P < 0.01$; Student's t test), whereas mEJC rise times were unchanged (control 1.20 ± 0.06 ms; $n = 10$; $drbp^{STOP1}$ 1.21 ± 0.07 ms, $n = 10$; $P = 0.9$; Student's t test). Thus, evoked SV fusion events in *drbp* mutants appeared desynchronized with the invasion of the presynaptic terminal by an AP. Because this synchronization depends on the spatiotemporal pattern of AP-triggered Ca^{2+} influx into the nerve terminal (21), changes in the abundance of Ca^{2+} channels might contribute to the observed defect. Indeed, Ca^{2+} channel signals, as evaluated by expression of Cac^{GFP} (5, 22), were slightly but consistently reduced by ~25% measured over the whole NMJ in all three *drbp* null alleles (Fig. 4F) (control 100% ±

2, $n = 136$; $drbp^{STOP1}$ 74% ± 3, $n = 52$; $drbp^{STOP2}$ 80% ± 3, $n = 19$; $drbp^{STOP3}$ 70% ± 3, $n = 45$). For the *drbp* hypomorph, Ca^{2+} channel signal was reduced by about 25% as well (Fig. 4F) ($drbp^{Minos}$ 71% ± 1, $n = 27$; $P < 0.001$, Mann-Whitney U test), whereas the evoked response was only reduced to 44% (Fig. 3A). Measuring Cac^{GFP} intensity per postsynaptic density (PSD) yielded a slightly stronger 36% decrease in $drbp^{STOP1}$ animals compared with controls (control 100% ± 4, $n = 48$ NMJs; $drbp^{STOP1}$ 64% ± 3, $n = 52$; $P < 0.001$, Mann-Whitney U test). This decrease in Ca^{2+} channel signal intensity was reflected by a ~30% decrease in calcium influx in response to single APs as determined by the $\Delta F/F$ amplitude of spatially averaged Ca^{2+} signals recorded from $drbp^{STOP1}$ mutant boutons (Fig. 4E) (control: 0.85 ± 0.06, $n = 20$ boutons; $drbp^{STOP1}$ 0.57 ± 0.03, $n = 44$ boutons; $P < 0.001$, Student's t test).

Consistent with previous findings in mammals (6, 7, 23) we found a biochemical interaction between DRBP and both *Drosophila* Ca^{2+}

channel α1 subunit Cac (yeast two-hybrid, human embryonic kidney (HEK) cell culture membrane recruitment assay) (fig. S6) and the *Drosophila* homolog of AZ protein RIM (yeast two-hybrid) (fig. S6, A and B). Interactions were specifically mediated by highly homologous PXXP motifs that bind to the third DRBP SH3 domain (fig. S6, A and B). Recently, RIM has been suggested to tether Ca^{2+} channels to the AZ membrane by means of (i) a direct interaction with the Ca^{2+} channel α1 subunit and (ii) an interaction with RBP (23). Mouse *rim-1* and *rim-2* double knockouts (DKOs) (23, 24), however, showed a rather moderate reduction in SV release in comparison with the dramatic *drbp* null phenotype. Thus, DRBP might bundle multiple interactions that are not necessarily downstream of RIM. Mechanistically, loss of DRBP leads to defects in Ca^{2+} channel abundance, Ca^{2+} influx, SV docking, and cytomatrix organization that probably all contribute to the severity of the *drbp*-release deficit.

Of note, in Bruchpilot mutants, cytomatrix and Ca^{2+} channel clustering defects are more

Fig. 4. *drbp* mutants show altered short-term synaptic transmission and deficits in Ca^{2+} channel abundance. (**A**) (Top) Sample traces of paired pulse stimulation for control (black) and *drbp*^{STOP1} (gray). (Bottom) Paired pulse ratio was significantly increased in *drbp*^{STOP1} at 30 ms, as well as 10 ms interstimulus interval (ISI) ($P < 0.001$ for 30 ms ISI; $P < 0.001$ for 10 ms ISI; Student's t test). (**B**) (Top) Sample traces of 10-Hz stimulation for control (black) and *drbp*^{STOP1} (gray). (Bottom) Mean eEJC amplitudes are plotted in bins of two (controls: closed symbols, $n = 10$; *drbp*^{STOP1}: open symbols, $n = 8$). (**C**) Sample traces of five-pulse stimulation at 100 Hz for control (black) and *drbp*^{STOP1} (gray) (top) and quantification (bottom) illustrate strong facilitation at *drbp*^{STOP1} NMJs. (**D**) *drbp*^{STOP1} eEJCs (left), but not mEJCs (right), had a significantly higher rise time than controls. (**E**) (Left) Confocal image showing 1b boutons filled with Oregon-Green 1,2-bis(2-aminophenoxy)ethane-*N*,*N*,*N′*,*N′*-tetraacetic acid–1 (BAPTA-1) and sample line scans across single boutons (dashed line, top) of single action-potential evoked spatially averaged Ca^{2+} transients (average of 10 scans). (Right) Changes in fluorescence quantified as $\Delta F/F$ revealed ~30% reduced peak amplitudes of evoked Ca^{2+} signals in *drbp*^{STOP1} mutants. Decay time constant τ remained unchanged (control: 150 ± 10 ms, $n = 20$; *drbp*^{STOP1} 153 ± 10 ms, $n = 44$; $P = 0.86$, Student's t test). Baseline fluorescence did not differ between genotypes. (**F**) Synapses of control animals, *drbp*^{STOP1} and *drbp*^{Minos} mutants were stained for Cac^{GFP} (green) and GluRIID (magenta). Ca^{2+} channel density was consistently reduced by about 25% measured over the whole NMJ in all mutant alleles. Measuring Cac^{GFP} intensity per PSD yielded a slightly stronger decrease in *drbp*^{STOP1} animals. Scale bar: 2 μm. Means ± SEM.
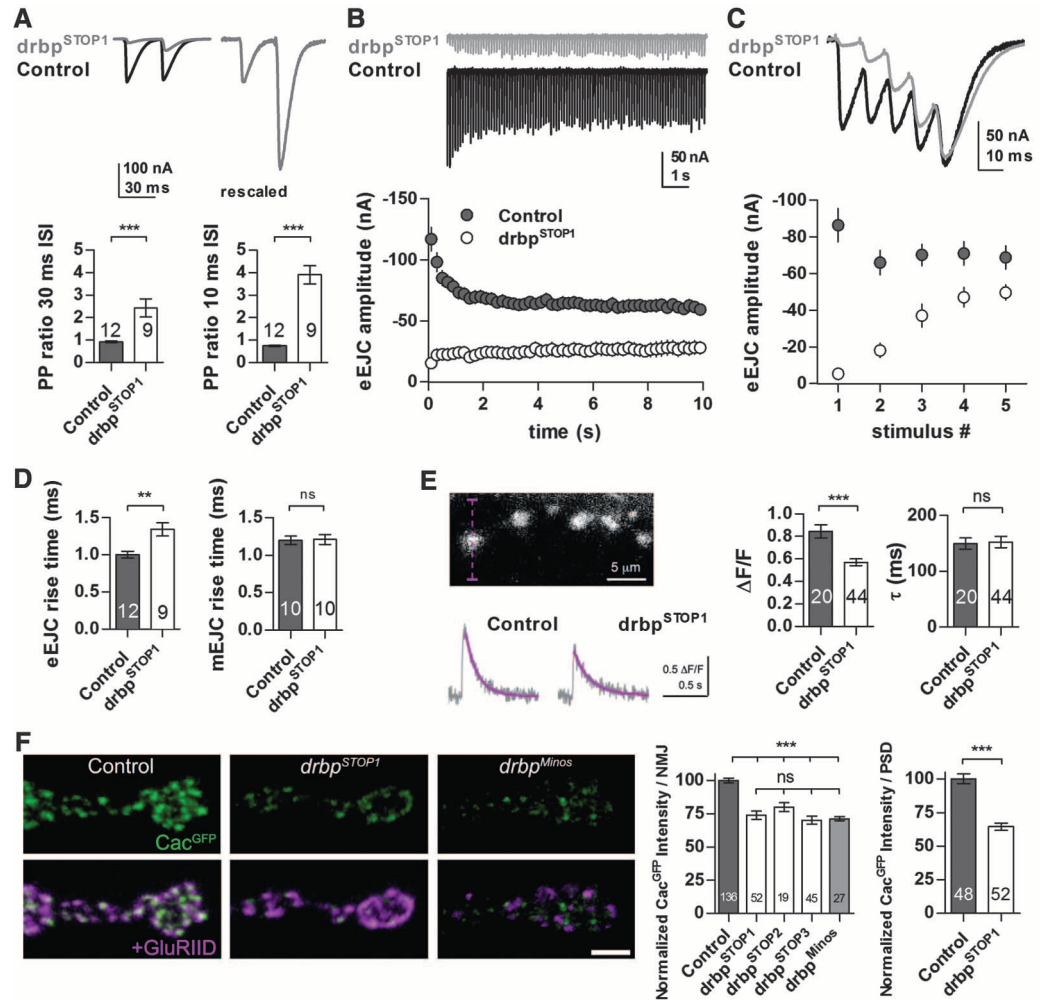
pronounced than in *drbp* nulls (*5*, *14*). Functionally, *drbp* and *bruchpilot* phenotypes appear similar: Both demonstrate decreased and desynchronized evoked SV release with atypical short-term facilitation. However, the deficits in evoked SV release are much more severe in *drbp* nulls than in *bruchpilot* nulls [i.e., release occurs at 5% versus 30% (*5*) of the respective wild-type level]. DRBP levels were clearly reduced in *bruchpilot* mutants (fig. S7), whereas gross Bruchpilot levels were not altered in *drbp* mutants (Fig. 2B). Given that even a partial loss of DRBP causes marked reduction in SV release (Fig. 3A), deficits in *bruchpilot* mutants might be explained, at least in part, by a concomitant loss of DRBP, and DRBP probably serves functions beyond the structural and Ca^{2+} channel–clustering roles of Bruchpilot.

Taken together, we identified DRBP as a central part of the AZ cytomatrix. How, in detail, DRBP functionally integrates into this protein network is subject to future analyses. Notably, the short-term plasticity phenotype of *drbp* mutants is reminiscent of mammalian *munc13-1* KO and *caps-1* and *caps-2* DKO mutants (*25*, *26*), which implicates functional links between priming factors and DRBP. Consistent with the functional importance of the DRBP protein family suggested by our study, human genetics recently identified

two *rbp* loci associated with autism with high confidence (*27*, *28*).

References and Notes

1. Y. Jin, C. C. Garner, *Annu. Rev. Cell Dev. Biol.* **24**, 237 (2008).
2. S. J. Sigrist, D. Schmitz, *Curr. Opin. Neurobiol.* **21**, 144 (2011).
3. S. Schoch, E. D. Gundelfinger, *Cell Tissue Res.* **326**, 379 (2006).
4. L. Siksou, A. Triller, S. Marty, *Curr. Opin. Neurobiol.* **21**, 261 (2011).
5. R. J. Kittel *et al.*, *Science* **312**, 1051 (2006).
6. Y. Wang, S. Sugita, T. C. Sudhof, *J. Biol. Chem.* **275**, 20033 (2000).
7. H. Hibino *et al.*, *Neuron* **34**, 411 (2002).
8. S. A. Spangler, C. C. Hoogenraad, *Biochem. Soc. Trans.* **35**, 1278 (2007).
9. T. Mittelstaedt, S. Schoch, *Gene* **403**, 70 (2007).
10. S. W. Hell, *Science* **316**, 1153 (2007).
11. J. Bückers, D. Wildanger, G. Vicidomini, L. Kastrup, S. W. Hell, *Opt. Express* **19**, 3130 (2011).
12. J. Hou, T. Tamura, Y. Kidokoro, *J. Neurophysiol.* **100**, 2833 (2008).
13. F. Kawasaki, R. Felling, R. W. Ordway, *J. Neurosci.* **20**, 4885 (2000).
14. W. Fouquet *et al.*, *J. Cell Biol.* **186**, 129 (2009).
15. F. Kawasaki, S. C. Collins, R. W. Ordway, *J. Neurosci.* **22**, 5856 (2002).
16. K. J. Venken, Y. He, R. A. Hoskins, H. J. Bellen, *Science* **314**, 1747 (2006).
17. L. Siksou *et al.*, *J. Neurosci.* **27**, 6868 (2007).
18. P. Rostaing, R. M. Weimer, E. M. Jorgensen, A. Triller, J. L. Bessereau, *J. Histochem. Cytochem.* **52**, 1 (2004).
19. S. Hallermann *et al.*, *J. Neurosci.* **30**, 14340 (2010).
20. E. O. Gracheva, E. B. Maryon, M. Berthelot-Grosjean, J. E. Richmond, *Front. Synaptic Neurosci.* **2**, 141 (2010).
21. E. Neher, T. Sakaba, *Neuron* **59**, 861 (2008).
22. F. Kawasaki, B. Zou, X. Xu, R. W. Ordway, *J. Neurosci.* **24**, 282 (2004).
23. P. S. Kaeser *et al.*, *Cell* **144**, 282 (2011).
24. Y. Han, P. S. Kaeser, T. C. Südhof, R. Schneggenburger, *Neuron* **69**, 304 (2011).
25. C. Rosenmund *et al.*, *Neuron* **33**, 411 (2002).
26. W. J. Jockusch *et al.*, *Cell* **131**, 796 (2007).
27. M. Bucan *et al.*, *PLoS Genet.* **5**, e1000536 (2009).
28. D. Pinto *et al.*, *Nature* **466**, 368 (2010).

Inhibitory Plasticity Balances Excitation and Inhibition in Sensory Pathways and Memory Networks

T. P. Vogels,[1]*† H. Sprekeler,[1]* F. Zenke,[1] C. Clopath,[1,2] W. Gerstner[1]

Cortical neurons receive balanced excitatory and inhibitory synaptic currents. Such a balance could be established and maintained in an experience-dependent manner by synaptic plasticity at inhibitory synapses. We show that this mechanism provides an explanation for the sparse firing patterns observed in response to natural stimuli and fits well with a recently observed interaction of excitatory and inhibitory receptive field plasticity. The introduction of inhibitory plasticity in suitable recurrent networks provides a homeostatic mechanism that leads to asynchronous irregular network states. Further, it can accommodate synaptic memories with activity patterns that become indiscernible from the background state but can be reactivated by external stimuli. Our results suggest an essential role of inhibitory plasticity in the formation and maintenance of functional cortical circuitry.

The balance of excitatory and inhibitory membrane currents that a neuron experiences during stimulated and ongoing activity has been the topic of many studies (*1–11*). This balance, first defined as equal average

[1]School of Computer and Communication Sciences and Brain-Mind Institute, École Polytechnique Fédérale de Lausanne, 1015 Lausanne EPFL, Switzerland. [2]CNRS, UMR 8119, Université Paris Descartes, 45 Rue des Saints Pères, 75270 Paris Cedex 06, France.

*These authors contributed equally to this work.
†To whom correspondence should be addressed. E-mail: tim.vogels@epfl.ch

amounts of de- and hyperpolarizing membrane currents (from here on referred to as "global balance"), is essential for maintaining stability of cortical networks (*1*, *2*). Balanced networks display asynchronous irregular (AI) dynamics that mimic activity patterns observed in cortical neurons. Such asynchronous network states facilitate rapid responses to small changes in the input (*2*, *3*, *12*), providing an ideal substrate for cortical signal processing (*4*, *13*, *14*).

Moreover, input currents to cortical neurons are not merely globally balanced but also coupled in time (*5*, *6*, *15*) and cotuned for different stim-

ulus features (*7*, *8*). The tight coupling of excitation and inhibition suggests a more precise, detailed balance, in which each excitatory input arrives at the cell together with an inhibitory counterpart (Fig. 1A), permitting sensory inputs to be transiently (*9*) or persistently turned on by targeted disruptions of the balance (*10*, *11*).

Although the excitatory-inhibitory balance plays an important role for stability and information processing in cortical networks, it is not understood by which mechanisms this balance is established and maintained during ongoing sensory experiences. Inspired by recent experimental results (*7*), we investigated the hypothesis that synaptic plasticity at inhibitory synapses plays a central role in balancing the excitatory and inhibitory inputs a cell receives.

We simulated a single postsynaptic integrate-and-fire neuron receiving correlated excitatory and inhibitory input signals. The cell received input through 1000 synapses (Fig. 1B), which were divided into eight independent groups of 100 excitatory and 25 inhibitory synapses. All excitatory and inhibitory synapses within each group followed the same temporally modulated rate signal (time constant τ ~ 50 ms) to mimic ongoing sensory activity (*13*, *16*). Spikes were generated from independent Poisson processes, leading to 125 different spike trains per signal. This architecture allowed each signal to reach the cell simultaneously through both excitatory and inhibitory synapses (Fig. 1B). To mimic glutamatergic and γ-aminobutyric acid (GABAergic) transmission, the synapses were conductance-based